Highly Stable Sb/C Anode for K^+ and Na^+ Energy Storage Enabled by Pulsed Laser Ablation and Polydopamine Coating

Hui Gao,[†] *Jeongyeon Lee,*[†] *Qixiao Lu, Yoonbin Kim, Kang Ho Shin, Ho Seok Park, Zhonghua Zhang,* and Lawrence Yoon Suk Lee**

Dr. H. Gao, Q. Lu, Prof. L. Y. S. Lee
Department of Applied Biology and Chemical Technology and Research Institute for Smart Energy, The Hong Kong Polytechnic University
Hung Hom, Kowloon, Hong Kong SAR, China
E-mail: lawrence.ys.lee@polyu.edu.hk

Dr. J. Lee
School of Fashion and Textiles, The Hong Kong Polytechnic University
Hung Hom, Kowloon, Hong Kong SAR, China

Dr. Y. Kim, K. H. Shin, Prof. H. S. Park
School of Chemical Engineering, Sungkyunkwan University, Suwon, Republic of Korea

Prof. Z. Zhang
Key Laboratory for Liquid-Solid Structural Evolution and Processing of Materials, School of Materials Science and Engineering, Shandong University, Jingshi Road 17923, Jinan 250061, China
E-mail: zh_zhang@sdu.edu.cn

[†] These authors contributed equally.

Abstract:

Potassium- and sodium-ion batteries (PIBs and SIBs) have great potential as the next-generation energy application owing to the natural abundance of K and Na. Antimony (Sb) is a suitable alloying-type anode for PIBs and SIBs due to its high theoretical capacity and proper operation voltage, yet the severe volume variation remains a challenge. Herein, we report a preparation of N-doped carbon-wrapped Sb nanoparticles (L-Sb/NC) using pulsed laser ablation and polydopamine coating techniques. As the anode for PIB and SIB, the L-Sb/NC delivers superior rate capabilities and excellent cycle stabilities (442.2 and 390.5 mA h g^{-1} after 250 cycles with the capacity decay of 0.037 and 0.038 % per cycle) at the current densities of 0.5 and 1.0 A g^{-1}, respectively. *Operando* X-ray diffraction reveals the facilitated and stable potassiation and sodiation mechanisms of L-Sb/NC enabled by its optimal core/shell structure. Furthermore, the SIB full cell fabricated with L-Sb/NC and $Na_3V_2(PO_4)_2F_3$ shows outstanding electrochemical performances, demonstrating its practical energy storage application.

Keywords: antimony nanoparticle; potassium-ion battery; sodium-ion battery; anode; laser ablation

1. Introduction

Li-ion battery (LIB) is in high demand because of the growing markets of portable electronics, electric vehicles, and large-scale grid storage. However, the uneven distribution and restricted reserves of Li resources are the main bottlenecks of the continued availability of LIBs. K- and Na-ion-based energy storages are attractive alternatives owing to their natural abundance, cost-effectiveness, appropriate reduction potentials, and suitable electrochemical behavior similar to Li.[1-3] However, the large ionic radius of K^+ and Na^+ causes structural failure and slow kinetics of K-ion batteries (PIBs) and Na-ion batteries (SIBs) during the repeated (de)potassiation and (de)sodiation, resulting in fading capacity and poor cycle stability.

To tackle these challenges, enormous efforts have been devoted to the optimization of electrode materials. The well-established LIB cathodes can be adopted to PIBs and SIBs,[4-6] but novel anode materials for PIBs need to be explored because the graphite anode of LIBs delivers poor rate capability in PIBs and almost no storage capability in SIBs.[7-8] So far, various anode candidates, including intercalation, conversion, and alloying materials, have been investigated for PIBs and SIBs. Intercalation-type anodes such as C- and Ti-based materials show good cycle stabilities yet suffer from intrinsically low capacity.[9] Although the conversion-type anodes including transition metal compounds can provide a high specific capacity, they are restricted by the large volume expansion and high working potential.[10] Recently, various alloying anodes, such as Sb, Bi, and Sn, have drawn great attention as promising anodes for PIBs and SIBs owing to their proper working potential and high theoretical specific capacity.[11-12] Among the alloying anodes, Sb has been regarded as one of the most potential materials owing to its high theoretical gravimetric and volumetric capacities (660 $mA\ h\ g^{-1}$ and 1,889 $mA\ h\ cm^{-3}$), low-stacking-density puckered-layer structure, and low cost (3-7 US$ per lb).[13-14] Nevertheless, the severe volume expansion during the (de)alloying due to the large radius sizes of K^+ and Na^+, which leads to pulverization, unstable solid electrolyte interphase (SEI), capacity decay, and low Coulombic efficiency, is still a challenge.

Various synthetic methods of nanosized Sb particles, hybridization of Sb with carbon materials, and carbon coating techniques have been suggested to facilitate ion and electron transfers and enhance structural stability during cycling.[12, 15] In particular, the Sb nanoparticle/carbon nanofiber composite demonstrated a high specific capacity of 393 mA h g^{-1} after 100 cycles at 0.2 A g^{-1} when employed as the anode in a PIB.[16] The construction of nano-structured Sb is an effective way to counteract its volume change, and many physical and chemical techniques, including ball-milling, templating, coprecipitation, and hydrothermal methods, have been utilized.[15, 17-18] However, most, if not all, methods require toxic solvents and/or additives during the synthetic procedure.

Herein, we report the synthesis of Sb nanoparticles coated with N-doped carbon (L-Sb/NC) using the laser ablation in liquids (LAL) and polydopamine (PDA) coating strategy. The LAL is a rapid and scalable technique that enables the facile synthesis of various nanosized- or few-layered materials from their bulk counterparts.[22-27] As a bioinspired synthetic polymer, PDA has been recently engaged in many applications, offering a controllable polymerization on various types of substrates under mild conditions.[19-21] The laser-ablated Sb nanoparticles in water were coated with an optimum thickness of PDA and annealed to yield L-Sb/NC in a core/shell configuration. The PDA-derived N-doped carbon shell improves the structural stability of the Sb core and facilitates the transport of ions and electrons by N dopant. When engaged as the anodes in PIB and SIB, the L-Sb/NC delivers excellent electrochemical performances by successfully balancing the specific capacity and cycling durability under relatively high current densities, outperforming other recently reported anode materials. The reversible potassiation and sodiation mechanisms as well as the electrochemistry-driven amorphization of Sb are revealed by *operando* X-ray diffraction (XRD), and the potential of L-Sb/NC anode in practical application is demonstrated with a full cell fabricated with

$Na_3V_2(PO_4)_2F_3$ cathode.

2. Experimental Section

Materials: Sb target (99.9 wt.%, diameter and thickness: 50.8 and 6.0 mm, respectively) was purchased from Beijing Dream Material Technology Company and polished to remove the surface oxide layer. Tris(hydroxymethyl)aminomethane ($NH_2C(CH_2OH)_3$, 99 wt.%) was purchased from Shenzhen Dieckmann Tech, China, and dopamine hydrochloride ($(HO)_2C_6H_3(CH_2)_2NH_2 \cdot HCl$, 98 wt.%) was purchased from Shanghai Aladdin Biochemical Technology Co. Ltd., China. Cu foil, conductive carbon black (Super P), poly(vinylidene fluoride) (PVDF), and carboxymethyl cellulose (CMC) were purchased from MTI Korea Corp. Na and K foils (99.9 wt. %) were purchased from Sigma–Aldrich, USA. Potassium trifluoromethane sulfonimide (KFSI, 3 M) in 1,2-dimethoxyethane (DME) and sodium trifluoromethane sulfonimide (NaTFSI, 1 M) in a mixture (1:1 vol.%) of propylene carbonate (PC) and fluoroethylene carbonate (FEC) were obtained from DodoChem, China. All chemicals were used without further treatment unless stated otherwise.

Pulsed laser-assisted ablation of Sb: A Nd:YAG Q-switched pulsed laser (wavelength = 1,064 nm, Nimma-600 Laser system) with an energy output of 320 mJ (650 V) and energy stability (root mean square) ≤ 1% was purchased from Beamtech Optronics Co. Ltd., China. The diameter of the beam was *ca*. 8 mm, and the distance between the surfaces of the Sb target and liquid (deionized (DI) water) was set as 12 mm. The Sb target was laser-ablated under continuous stirring at 20 °C for 6 h to yield a uniform suspension of L-Sb_2O_3 (concentration = *ca*. 0.2 − 0.3 mg mL^{-1}), which was collected as a powder by vacuum filtering and drying at 60 °C under vacuum.

Synthesis of L-Sb/NC: Tris(hydroxymethyl)aminomethane (10 mM) and dopamine hydrochloride (1 mg mL^{-1}) were added to the L-Sb_2O_3 suspension (100 mL, 1 mg mL^{-1}) and stirred at room temperature for polymerization (denoted as L-Sb_2O_3@PDA-X, where X represents polymerization time). The polymerized L-Sb_2O_3 suspension was washed with DI water, collected by vacuum filtration, and dried at 60 °C in a vacuum oven. The PDA-coated samples were annealed at 450 °C in a tube furnace under Ar/H_2 atmosphere (10 vol.% of H_2) for 2 h to fabricate the L-Sb/NC samples (denoted as L-Sb/NC-X, where X represents polymerization time).

Microstructural Characterization: The crystal structure of the samples was characterized by an X-ray diffractometer (Rigaku SmartLab 9 kW Advance, voltage 45 kV, current 200 mA) equipped with Cu Kα radiation. The morphology of the samples was probed by scanning electron microscopy (SEM, Tescan VEGA3) and field emission SEM (FESEM, Tescan MAIA3). An energy-dispersive X-ray spectra (EDS) analyzer coupled with SEM was used to determine the chemical composition of the samples. Transmission electron microscopy (TEM, JEOL system (Model JEM-2100F, 200 kV)) was utilized to characterize the microstructures of the as-prepared samples. The TEM samples were prepared by drop-casting sample solution on a Cu grid. X-ray photoelectron spectroscopy (XPS) was conducted using a Thermo Fisher ESCALAB 250Xi system. The spectrometer was calibrated and fitted using the XPSPEAK41 with the C 1s peak at 284.6 eV. Raman spectra were acquired by a Witec confocal Raman system (alpha300R) with the excitation laser (λ = 532 nm) of 5 mW energy for all tests to minimize sample burning. Thermogravimetric analyses (TGA) were performed on a thermal analyzer (TA Instruments TGA 5500) at a heating rate of 10 °C min^{-1} in N_2 and air. The zeta potentials of samples were determined by Malvern Zetasizer Nano ZS90. The size distribution was measured using the Nano Measure software (Version 1.2.5).

Battery Cell Assembly: All electrodes were fabricated by a scrapping-coating method. A slurry was prepared by mixing the active material powders, Super P, and CMC binder with a weight ratio of 7:2:1 in DI water, followed by stirring for approximately 12 h. The slurry was coated onto a stainless-steel mesh (type 304, thickness = 0.1 mm) for *operando* XRD or a Cu foil for other electrochemical measurements. The coated electrodes were dried at 80 °C for 12 h in a vacuum and then cut into a disk ($d = 10$ mm) with a mass loading of *ca*. 1.0 mg cm^{-2}. The as-prepared electrode was engaged as the working electrode, while Na or K foil was used as both the counter and reference electrodes, and glass fiber (GF/D, Whatman) served as the separator. The electrolytes were 3 M KFSI in DME for PIBs and 1 M NaTFSI in a mixed solvent of PC and FEC (1:1 vol.%) for SIBs. The CR2032 cell was assembled in an Ar-filled glove box and aged for 24 h before the test. For *operando* XRD, a special CR2032 coin cell that was equipped with Be window ($d = 10$ mm) on one side was used. XRD patterns were collected based on a "time step" method at 0.05 A g^{-1}. In the time step mode, the scan rate of XRD was determined by the count time for each degree point to obtain the distinct XRD peaks. The count time of eight seconds per one degree was used in our work. For the post-TEM analysis after cycling, the cycled coin cells were first disassembled in an argon-filled glove box. The electrode materials were washed with diethyl carbonate to remove residual sodium or potassium salt and peeled off from the current collectors, followed by dispersing in ethanol by ultrasonication for TEM analysis.

For the full battery test, $Na_3V_2(PO_4)_2F_3$ mixed with Super P and PVDF binder (7:2:1 by weight) was cast on Al foil and used as the cathode. The L-Sb/NC electrode described above was adopted as the anode. The weight ratio of active material in the cathode to that in the anode was balanced and set at 2.8:1. The mass loadings of $Na_3V_2(PO_4)_2F_3$ cathode and L-Sb/NC anode were *ca*. 1.4 − 2.0 and 0.5 − 0.7 mg cm^{-2}, respectively. The same electrolyte used in the half-cell was also used for the full battery.

Battery Cell Test: Galvanostatic measurements and galvanostatic intermittent titration technique (GITT) were performed on a test system (Xinwei CT-4008Tn-5V50mA battery testing system) by tautologically applying short pulses (current density = 0.05 A g^{-1}) for 1,800 s and an open-circuit stand for 7,200 s for complete relaxation to achieve equilibrium potentials during cycling. Cyclic voltammograms (CVs) were collected using a WonATech battery testing system (WBCS3000L). Electrochemical impedance spectroscopy (EIS) was performed at the open-circuit voltage (OCV) using a PARSTAT MC (PMC1000/DC) electrochemical system (Princeton Applied Research, USA). The frequency range was set from 10 mHz to 100 kHz with an excitation voltage of 5 mV.

3. Results and discussion

Figure 1a illustrates the synthetic procedure of L-Sb_2O_3 nanoparticles, and the experimental setup is shown in **Figure S1**. Briefly, the bulk Sb target placed in DI water was directly irradiated by an Nd:YAG Q-switched pulsed laser (λ = 1,064 nm, 320 mJ). Upon irradiation, the initially transparent solution changes to a white suspension of well-dispersed L-Sb_2O_3 nanoparticles. The pulsed laser generates plasma from the Sb target, which has a short lifetime from a few ns to μs. The plasma energy is transferred to the solvent molecules, forming vapor bubbles surrounding the plasma and accelerating the motion of molecules in the solvent.[25] From the repeated processes, nanosized Sb species are produced by the plasma energy and the bubbling effect in the solvent.[28-30] The laser-ablated Sb nanoparticles were first oxidized to L-Sb_2O_3 by the oxygen in the water and coated with carbon shells *via* the polymerization strategy using dopamine. Polydopamine (PDA)-derived carbon coatings have been applied on various metal and semiconductor surfaces to improve structural stability and electrical conductivity.[31] The heat treatment (450 °C) of L-Sb_2O_3@PDA in Ar/H_2 atmosphere yields a core/shell structure of Sb nanoparticle encapsulated with N-doped carbon (L-Sb/NC). The synthetic procedure is described in detail in the Experimental Section.

X-ray diffraction (XRD) patterns of L-Sb_2O_3 and L-Sb_2O_3@PDA confirm the Sb_2O_3 phase (JCPDS # 43-1071, **Figure 1b**), and the two small peaks at 25.0 and 26.5° observed from L-

Sb_2O_3@PDA correspond to the amorphous structure of PDA layer.[32] All the XRD peaks of L-Sb/NC are indexed to the Sb phase (JCPDS # 35-0732) except for a tiny Sb_2O_3 peak at 27.7°, indicating an almost complete reduction of Sb_2O_3 to Sb by the annealing process. The scanning electron microscopic (SEM) images (**Figures 1c** and **S2**) of L-Sb_2O_3 and L-Sb/NC exhibit irregular particles with mean sizes of 77.2 ± 40.9 nm (**Figure S3**) and 142.6 ± 72.7 nm (**Figure 1c**), respectively. **Figures S4** and **S5** display the energy-dispersive X-ray (EDX) elemental mapping images of L-Sb_2O_3 and L-Sb/NC, and their Sb contents are 82.5 and 58.8 wt.%, respectively, as summarized in **Table S1**. Thermogravimetric analysis (TGA) was conducted to confirm the actual amount of Sb in L-Sb/NC (**Figure 2a**). The residual weight of 33.6 wt.% after the removal of carbon at >550 °C indicates that the actual amount of Sb is 62.3 wt.% based on the weight of the final product of Sb_2O_3,[33] which agrees well with the EDX result.

Raman spectroscopy was engaged to further investigate the structure of L-Sb/NC (**Figure 2b**). The two distinct peaks at *ca.* 110.9 and 147.5 cm^{-1} are assigned to the metallic Sb[34] while a weak and broad peak at *ca.* 269.8 cm^{-1} is attributed to the trace amount of Sb_2O_3 in L-Sb/NC.[35] Two other prominent peaks at *ca.* 1,366.7 and 1,592.7 cm^{-1} are assigned to the D band (defects or disordered structure) and G band (ordered graphitic structure) of carbon species, respectively. Their intensity ratio (I_D/I_G) of 0.71 indicates the moderate graphitization of the carbon shell.[36-38] It is worth noting that such defective or disordered structures can act as the reactive site and promote ion transportation.[39-41]

X-ray photoelectron spectroscopy (XPS) was employed to investigate the elemental compositions and surface chemical states of the as-prepared samples. The survey XPS spectra (**Figure S6**) confirm the existence of C, Sb, O, and N elements in L-Sb/NC and L-Sb_2O_3@PDA. The high-resolution Sb 3*d* XPS spectrum of L-Sb/NC can be deconvoluted into two pairs of characteristic peaks corresponding to the Sb^{3+} (533.0 and 541.3 eV) and Sb^0 states (530.9 and 540.3 eV, **Figure 2c**), confirming the coexistence of Sb_2O_3 and metallic Sb.[42-43] The high-resolution C 1*s* spectrum of L-Sb/NC can be deconvoluted into three peaks that are assigned to C–C (284.7 eV), C=N (285.7 eV), and O=C–N (289.1 eV, **Figure S7c**).[31, 44] Two peaks observed at 399.0 and 400.5 eV from the N 1*s* spectrum are attributed to pyridinic N and pyrrolic N, respectively (**Figure S7e**). These N species that are present in the carbon matrix as dopants can promote electrical conductivity and wettability.[45] L-Sb_2O_3@PDA exhibits C 1*s* and N 1*s* spectra (**Figures S7d** and **S7f**). Three C 1*s* peaks at 284.6, 285.9, and 288.6 eV are assigned to C–C, C=N, and O=C–N, respectively, while two N 1*s* peaks at 399.5 and 400.3 eV are assigned to pyridinic N and pyrrolic N, respectively.

Zeta potential is a useful measure to probe the charge states of the surface. The zeta potential of L-Sb_2O_3 is measured as 53.5 ± 4.1 mV, a higher value than the general threshold (30 mV) for stable colloidal solutions, which indicates the excellent stability of the laser-ablated L-Sb_2O_3 suspension.[46-47] On the contrary, the L-Sb/NC shows a negative zeta potential of −12.2 ± 3.6 mV, which would be beneficial for the adsorption of the K^+ and Na^+ ions and electrochemical kinetics.[48]

The morphology and composition of L-Sb_2O_3@PDA and L-Sb/NC were confirmed by transmission electron microscopy (TEM, **Figures 2d** – **2h** and **S8**). The PDA coating affords a uniform (24.2 ± 2.5 nm) polymeric layer on L-Sb_2O_3@PDA (**Figures S9a** and **S8a** – **S8b**). Such core/shell structure is well retained in L-Sb/NC (**Figures 2e** and **S8c** – **S8f**), where Sb nanoparticles (d = 108.7 ± 56.3 nm) are encapsulated with the carbon shell derived from PDA coating (25.8 ± 6.0 nm, **Figures S9b** and **S9c**). Notably, void spaces, which are created by the volumetric contraction during the conversion of Sb_2O_3 to Sb[49] as well as the partial decomposition of PDA, are observed between the Sb nanoparticles and carbon shell of L-Sb/NC.[20, 44] The lattice fringes showing the *d*-spacings of 3.16 and 3.05 Å, which are attributed to the (222) plane of Sb_2O_3 and the (012) plane of Sb, respectively, are apparent in the high-resolution TEM image of L-Sb/NC (**Figures 2f** and **S8e** – **S8f**). The Sb_2O_3 phases of L-

Sb_2O_3@PDA are also confirmed with the *d*-spacings of 3.16 Å from their high-resolution TEM images (**Figure S8b**). The selected-area electron diffraction (SAED) pattern of L-Sb/NC indicates its crystalline state, and the observed pattern is assigned to the lattice planes of (012), (110), and (104) of Sb (**Figure 2g**). Scanning TEM (STEM) image and the corresponding elemental mapping images of L-Sb/NC clearly reveal the core/shell structure with void spaces and the even distribution of C, O, N, and Sb (**Figure 2h**).

The electrochemical performance of L-Sb/NC as the anode in PIB was first evaluated by cyclic voltammetry (CV) in the potential window between 0.01 and 2.0 V (*vs.* K^+/K) at a scan rate of 0.05 mV s^{-1} (**Figure 3a**). Two broad reduction peaks are observed at *ca.* 0.17 (peak 2-R) and 0.04 V (peak 3-R) in the first cycle, which are attributed to the formation of solid electrolyte interphase (SEI) and the potassiation of L-Sb/NC, respectively. Two oxidation peaks at *ca.* 0.73 and 1.19 V (peaks 1-O and 2-O, respectively) in the anodic scan correspond to the depotassiation process. In the subsequent cycles, the recurring cathodic (*ca.* 0.55 (peak 1-R) and 0.12 V) and anodic peaks (*ca.* 0.72 and 1.16 V) indicate a stable redox reaction. The galvanostatic discharge–charge profile of the L-Sb/NC anode recorded at a current density of 0.5 A g^{-1} for 250 cycles displays typical sloping plateaus that are related to the alloying reaction of Sb (**Figure 3b**).[50] In the first discharge and charge cycle, the specific capacities of 810.8 and 546.5 mA h g^{-1} are measured, respectively, with a Coulombic efficiency of 67.4 % owing to the irreversible capacity loss by the initial SEI formation. Both discharge/charge curves gradually stabilize in the subsequent cycles, demonstrating superior stability of the L-Sb/NC electrode up to 250 cycles.

Figure 3c displays the cycle performance of the L-Sb/NC anode at a current density of 0.5 A g^{-1} for 250 cycles. The L-Sb/NC anode shows the specific capacities of 487.2 and 518.3 mA h g^{-1} in the 2nd and 124th cycles, respectively, due to the initial activation behavior.[51] At the end of 250 cycles, the L-Sb/NC anode still retains the reversible capacity of 442.2 mA h g^{-1}

with a capacity loss of merely 0.037 % per cycle, which indicates remarkable cycle stability. The rate capability and the corresponding galvanostatic curves of the L-Sb/NC anode at various current densities are shown in **Figures 3d** and **S10**. The L-Sb/NC anode delivers the discharge capacities of 502.2, 487.1, 464.8, 445.4, and 367.7 mA h g^{-1} at 0.1, 0.2, 0.5, 1.0, and 2.0 A g^{-1}, respectively. Upon returning to a current density of 0.1 A g^{-1}, the discharge capacity of 517.1 mA h g^{-1} is recovered, which reveals a fast kinetics of the L-Sb/NC anode.

Electrochemical impedance spectroscopy (EIS) and galvanostatic intermittent titration technique (GITT) were engaged to investigate the electron diffusion and charge transfer of L-Sb/NC cells. **Figure 3e** exhibits the Nyquist plots of the pristine and cycled L-Sb/NC cells, which were analyzed by fitting the equivalent circuit (**Figure S11**). The Warburg factor was calculated by the relationship between Z' and $\omega^{-1/2}$, where Z' is the real part of the impedance and ω is the angular frequency (**Figure 3f**), to determine the diffusion coefficient of K^+ ion ($D_{\text{K-eis}}$) using the following equations;[52-53]

$$Z' = R_{ct} + R_e + \sigma\, \omega^{-1/2} \tag{1}$$

$$D_{\text{K}-\text{eis}} = \frac{R^2T^2}{2A^2n^4F^4{C_{\text{K}}}^2\sigma^2} \tag{2}$$

where R_{ct} is the charge transfer resistance of the electrode, R_e is the combination of electrical, ionic, and contact resistances, σ is the Warburg factor, R is the gas constant, T is temperature, n is number of electrons, A is surface area of electrode, F is the Faraday constant, and C_K is the concentration of K^+. The calculated results (**Table S2**) indicate that the R_{ct} of L-Sb/NC is reduced while its $D_{\text{K-eis}}$ value is increased after the first cycle, suggesting improved ion and electron transfers. The K^+ ion diffusion coefficient ($D_{\text{K-gitt}}$) can also be approximated from the GITT data using the following equation;[54-55]

$$D_{\text{K}-\text{gitt}} = \frac{4}{\pi\tau}\left(\frac{n_{\text{m}}\text{V}_{\text{m}}}{A}\right)^2\left(\frac{\Delta E_{\text{s}}}{\Delta E_{\tau}}\right)^2 \tag{3}$$

where τ is pulse duration, n_m is the number of moles, V_m is molar volume of the electrode, which was assumed to have a fixed value ignoring the volume variation,[49] A is interface area,

ΔE_τ is the voltage change during the constant current pulse, ΔE_s is the steady-state voltage change, and E_0 and E_s are the voltage values before and after the single-step GITT experiments, which can be calculated based on the GITT results, as shown in **Figures S12** and **S13**. **Figure 3g** shows that the $D_{\text{K-gitt}}$ values during the charging process (*ca.* 10^{-13} – 10^{-11} cm^2 S^{-1}) are higher than those during the discharging process (*ca.* 10^{-14} – 10^{-12} cm^2 S^{-1}). These values agree well with the linearly inclined reduction and oxidation peak currents (i_p) as the scan rate is increased (**Figures 3h** and **3i**).

Inspired by the remarkable potassium storage performance of the L-Sb/NC anode, we also investigated its electrochemical performance in SIB. **Figure 4a** exhibits the CVs of L-Sb/NC at 0.1 mV s^{-1} in the initial five cycles, which show redox peaks at 0.23, 0.09, and 0.95 V (*vs.* Na^+/Na) corresponding to Na^+ alloying/dealloying reactions. The theoretical capacity (C_L) of the L-Sb/NC in SIB is calculated to be 460.2 mA h g^{-1} by the following equation,

$$C_\text{L} = C_\text{p} \times \text{W}_\text{p} + C_\text{Sb} \times \text{W}_\text{Sb} \qquad (4)$$

where C_p and C_Sb are the theoretical capacities of PDA-derived carbon shell (130 mA h g^{-1}) and Sb (660 mA h g^{-1}),[56] respectively, and W_P and W_Sb are the contents of PDA-derived carbon shell (37.7 wt.%) and Sb (62.3 wt.%), respectively. L-Sb/NC delivers a superior cycling performance with the discharge capacities of 431.7 and 390.5 mA h g^{-1} in the 2nd and 250th cycles at 1.0 A g^{-1}, respectively, and a capacity decay of 0.038 % per cycle (**Figures 4b** and **4c**). The result of the rate capability test is shown in **Figure 4d** where the discharge capacities of 506.1, 478.8, 450.4, 435.1, 411.2, 395.5, 386.1, and 370.9 mA h g^{-1} are recorded at the current densities of 0.1, 0.2, 0.5, 1.0, 2.0, 3.0, 4.0, and 5.0 A g^{-1}, respectively. L-Sb/NC recovers the discharge capacity of 503.5 mA h g^{-1} upon returning to 0.1 A g^{-1}. The corresponding galvanostatic curves at various current densities are shown in **Figure S14**. EIS (**Figures 4e** and **4f**) and GITT (**Figures 4g** and **S15**) were performed to compare the ion diffusivity and charge transfer of L-Sb/NC in PIB and SIB. Based on the fitting results of EIS data (**Table S3**) and the

CVs at various scan rates (**Figure 4h**), the L-Sb/NC cell shows reduced R_{ct} and inclined $D_{Na\text{-}eis}$ after the first cycle, a result that is similar to the case of PIB. The peak current also displays a linear relationship with the scan rate (**Figure 4i**).

To understand the structural changes of L-Sb/NC during the first 100 cycles in PIB and SIB, TEM analysis was conducted after the cycling (**Figures 5a – 5d** and **S16**). From the TEM images of L-Sb/NC in both PIB and SIB, the interplanar spacing of the Sb (102) phase is observed and the core/shell structure is well maintained after 100 cycles (**Figures 5** and **S16**), which demonstrates the exceptional structural stability of L-Sb/NC owing to the protection of the carbon shells. Due to the transformation of Sb_2O_3 into amorphous K_2O/Na_2O and Sb during the initial discharge, the lattice fringes of Sb_2O_3 cannot be seen.[57-58] The effect of the N-doped carbon shell derived from the optimized PDA coating was verified by SEM analysis and electrochemical tests (**Figures S17 – S19**). L-Sb/NC-3h and L-Sb/NC-6h samples with thinner carbon shells show the aggregated and diffused Sb particles due to weak and broken carbon shells.[20, 59] In particular, the L-Sb/NC-6h electrode shows severe capacity fading due to the micro-sized Sb and the structural instability, delivering worse performance than the L-Sb/NC electrode (**Figure S18**). Two electrodes with thicker carbon shells, L-Sb/NC-18h and L-Sb/NC-24h, also display inferior cycle stability after 200 cycles than L-Sb/NC electrodes (**Figure S19**). In comparison with other recently reported anodes for PIB, L-Sb/NC realizes the best comprehensive electrochemical performances, successfully balancing the specific capacity and lifespan under high current density (**Figure 5e** and **Table S4**). The L-Sb/NC anode in SIB also achieves a high specific capacity that ranges between 84.9 and 93.8 % of the theoretical capacity and decent long-term endurance, showing a performance comparable to other similar anodes for SIBs (**Figure S20** and **Table S5**). Such remarkable K^+ and Na^+ storage ability is attributed to the following aspects: (i) Laser-induced nanoengineering of Sb shortens the solid-state ion diffusion distance, reducing the resistance and enhancing the kinetics.[60] (ii) The optimized N-doped carbon shell serves as a conductive pathway and buffer layer, while the N dopant enhances the charge transfer.[61-62] (iii) The voids created by the thermal conversion reaction of Sb_2O_3 to Sb offer the buffering space to mitigate the volume expansion of Sb.

To clarify the (de)potassiation mechanism of the L-Sb/NC electrode, *operando* XRD was used to track the phase changes during the initial two cycles (**Figure 6a**). The peaks at 23.7, 25.2, 28.7, 40.1, 41.9, 47.1, and 48.4° are assigned to Sb, and the peak at 27.7° is attributed to Sb_2O_3. During Stage 1 between OCV and 0.01 V (*vs.* K^+/K), these peaks gradually diminish and finally vanish in the middle of discharge (*ca.* 0.4 V). Afterward, the appearance and enhancement of peaks at 18.1, 20.9, 29.8, 35.0, 36.6, 42.6, and 46.6° that are indexed to the K_3Sb (JCPDS # 19-0935) can be observed. Such a process reflects the complete transformation from Sb and Sb_2O_3 to K_3Sb and amorphous K_2O *via* the immediate products of amorphous K_xSb and K_2O.[63-64] Upon further depotassiation (Stage 2 between 0.01 and 2.0 V), the depotassiation conversion from K_3Sb to amorphous Sb *via* amorphous K_xSb occurs without any new peaks appearing. This supports the hypothesis that the amorphization of Sb is driven by an electrochemical reaction. Such electrochemical amorphization of Sb can increase ion storage sites,[51] facilitate ion transfer,[65] and tolerate stress due to the isotropy property.[66] During the second cycle, only the peaks assigned to K_3Sb are observed, further confirming the similar two-step (de)alloying processes. The contour plot presented in **Figure 6b** illustrates the (de)potassiation procedure of the L-Sb/NC electrode during the cycling.

Operando XRD was also utilized to probe the (de)sodiation mechanism of the L-Sb/NC electrode (**Figure 6**). Similar to the two-step (de)alloying processes in PIB, a two-step transformation from Sb and Sb_2O_3 to Na_3Sb and Na_2O *via* the immediate products of amorphous Na_xSb and Na_2O is observed. Particularly, the progressive broadening of Sb peaks during the cycle suggests the electrochemical amorphous proliferation of the L-Sb/NC anode. The contour plot in **Figure 6d** demonstrates the corresponding (de)sodiation procedure. **Table**

S7 summarizes the (de)alloying mechanisms of the L-Sb/NC electrode during the cycling of PIB and SIB. *Ex situ* XPS was employed to investigate the post-cycle L-Sb/NC electrodes under various states (**Figures S21** and **S22**). All the Sb 3*d* XPS spectra of L-Sb/NC electrodes used in both PIB and SIB can be deconvoluted into the two characteristic peaks corresponding to the Sb^0 state (*ca.* 530.3 and 539.5 eV). The absence of Sb^{3+} peaks indicates the irreversible reduction of Sb_2O_3 during the 1st discharge, which agrees well with the results of the *operando* XRD (**Figure 6**). Meanwhile, the two peaks at *ca.* 531 and 533 eV are assigned to the O–C=O and C–O–C species of the CMC binder, respectively.[67]

Figure 7a shows the charge–discharge curves of L-Sb/NC/$Na_3V_2(PO_4)_2F_3$ full cell in the potential window between 2.0 and 4.3 V (*vs.* Na^+/Na) at the current density of 0.5 A g^{-1}. The full cell displays an initial discharge capacity of 102.4 mA h g^{-1} based on the mass of the cathode with a voltage plateau from 3.9 to 3.1 V and a flat voltage plateau until 2.8 V. The L-Sb/NC/$Na_3V_2(PO_4)_2F_3$ full cell shows a higher voltage plateau compared with the previously reported $MnFe_2O_4$@C/$Na_3V_2(PO_4)_2F_3$ (3.0 – 1.8 V)[68] and $MoS_{1.2}Se_{0.8}$@G/$Na_3V_2(PO_4)_2F_3$ (2.5 – 0.0V),[69] demonstrating good stability. From the CV curve of the full cell shown in **Figure S23**, three pairs of reduction and oxidation peaks are identified at *ca.* 3.08, 3.38, and 3.87 V, which are consistent with the corresponding charge–discharge curves. The full cell also shows a remarkable rate capability with the reversible capacities of 95.8, 86.9, 68.9, 52.9, and 35.2 mA h g^{-1} at the current densities of 1.0, 2.0, 5.0, 10, and 20 A g^{-1}, respectively (**Figure 7b**). The cycle performance of the SIB full cell in **Figure 7c** displays that the specific capacity of 103.9 mA h g^{-1} is well retained after 200 cycles at a current density of 1.0 A g^{-1}, achieving ~100 % capacity retention. **Figure 7c** displays the cycle performance of the SIB full cell. After 200 cycles, the discharge capacity retains the specific capacity of 103.9 mA h g^{-1} at a current density of 1.0 A g^{-1} with a capacity retention of 101.5 %, further confirming the exceptional cycle stability of L-Sb/NC for SIB.

4. Conclusions

In summary, L-Sb/NC was fabricated by a facile laser-ablation method and an optimized PDA-derived carbon coating technique as the alloying anode of high structural stability for PIBs and SIBs. When employed in PIB, the L-Sb/NC anode achieves a high initial specific discharge capacity of 487.2 mA h g^{-1} and long long-term durability with a capacity retention of 442.2 mA h g^{-1} over 250 cycles at 0.5 A g^{-1}, which are the best comprehensive K storage performances so far. As an anode in SIB, the L-Sb/NC also delivers excellent electrochemical performances. With the laser-assisted nanoengineering and the protection of a carbon shell by the PDA coating strategy, the kinetics of K^+ and Na^+ transports and structural stability during cycling are highly enhanced as proved by the *operando* XRD. The full cell test with $Na_3V_2(PO_4)_2F_3$ cathode delivers superior performances with a high specific capacity of 103.9 mA h g^{-1} after 200 cycles at 1.0 A g^{-1}, demonstrating the potential of L-Sb/NC anode in practical SIB application.

Acknowledgements

We gratefully acknowledge the financial support from the Research Grants Council of the Hong Kong SAR (PolyU15217521) and the Research Institute for Smart Energy of the Hong Kong Polytechnic University (Q-CDA3 and 1-W16K).

Appendix A. Supplementary data

Supplementary data to this article can be found online at

References

[1] N. Yabuuchi, K. Kubota, M. Dahbi, S. Komaba, *Chem. Rev.* **2014**, *114*, 11636.

[2] P. K. Nayak, L. Yang, W. Brehm, P. Adelhelm, *Angew. Chem. Int. Ed.* **2018**, *57*, 102.

[3] X. Min, J. Xiao, M. Fang, W. Wang, Y. Zhao, Y. Liu, A. M. Abdelkader, K. Xi, R. V. Kumar, Z. Huang, *Energy Environ. Sci.* **2021**, *14*, 2186.

[4] J. Xiao, X. Li, K. Tang, D. Wang, M. Long, H. Gao, W. Chen, C. Liu, H. Liu, G. Wang, *Mater. Chem. Front.* **2021**, *5*, 3735.

[5] Y.-S. Xu, S.-J. Guo, X.-S. Tao, Y.-G. Sun, J. Ma, C. Liu, A.-M. Cao, *Adv. Mater.* **2021**, *33*, 2100409.

[6] S. Liu, L. Kang, S. C. Jun, *Adv. Mater.* **2021**, *33*, 2004689.

[7] X. Li, J. Li, L. Ma, C. Yu, Z. Ji, L. Pan, W. Mai, *Energy Environ. Mater.* **2022**, *5*, 458.

[8] M. Dahbi, N. Yabuuchi, K. Kubota, K. Tokiwa, S. Komaba, *Phys. Chem. Chem. Phys.* **2014**, *16*, 15007.

[9] Y. Wu, H. Zhao, Z. Wu, L. Yue, J. Liang, Q. Liu, Y. Luo, S. Gao, S. Lu, G. Chen, X. Shi, B. Zhong, X. Guo, X. Sun, *Energy Stor. Mater.* **2021**, *34*, 483.

[10] Y. Fang, D. Luan, X. W. Lou, *Adv. Mater.* **2020**, *32*, 2002976.

[11] M. Lao, Y. Zhang, W. Luo, Q. Yan, W. Sun, S. X. Dou, *Adv. Mater.* **2017**, *29*, 1700622.

[12] I. Sultana, M. M. Rahman, Y. Chen, A. M. Glushenkov, *Adv. Funct. Mater.* **2018**, *28*, 1703857.

[13] K. Subramanyan, V. Aravindan, *Chem* **2019**, *5*, 3096.

[14] H. Gao, X. Guo, S. Wang, F. Zhang, H. Liu, G. Wang, *EcoMat* **2020**, *2*, e12027.

[15] S. Imtiaz, I. S. Amiinu, Y. Xu, T. Kennedy, C. Blackman, K. M. Ryan, *Mater. Today* **2021**, *48*, 241.

[16] X. Ge, S. Liu, M. Qiao, Y. Du, Y. Li, J. Bao, X. Zhou, *Angew. Chem. Int. Ed.* **2019**, *58*, 14578.

[17] W. T. Jing, C. C. Yang, Q. Jiang, *J. Mater. Chem. A* **2020**, *8*, 2913.

[18] S. Sarkar, S. C. Peter, *J. Mater. Chem. A* **2021**, *9*, 5164.

[19] J. Kong, W. A. Yee, L. Yang, Y. Wei, S. L. Phua, H. G. Ong, J. M. Ang, X. Li, X. Lu, *Chem. Commun.* **2012**, *48*, 10316.

[20] Y. Liu, K. Ai, L. Lu, *Chem. Rev.* **2014**, *114*, 5057.

[21] M. E. Lynge, R. van der Westen, A. Postma, B. Städler, *Nanoscale* **2011**, *3*, 4916.

[22] L. H. Reddy, J. L. Arias, J. Nicolas, P. Couvreur, *Chem. Rev.* **2012**, *112*, 5818.

[23] N. Kamboj, T. Purkait, M. Das, S. Sarkar, K. S. Hazra, R. S. Dey, *Energy Environ. Sci.* **2019**, *12*, 2507.

[24] P. A. Doble, R. G. de Vega, D. P. Bishop, D. J. Hare, D. Clases, *Chem. Rev.* **2021**, *121*, 11769.

[25] W. Zheng, J. Lee, Z.-W. Gao, Y. Li, S. Lin, S. P. Lau, L. Y. S. Lee, *Adv. Energy Mater.* **2020**, *10*, 1903490.

[26] J. Lee, H. Song, K.-A. Min, Q. Guo, D. Kim, Z. Zheng, B. Han, Y. Jung, L. Y. S. Lee, *Small Methods* **2021**, *5*, 2100215.

[27] C. Chen, Y. Kuang, L. Hu, *Joule* **2019**, *3*, 683.

[28] H. Zeng, X.-W. Du, S. C. Singh, S. A. Kulinich, S. Yang, J. He, W. Cai, *Adv. Funct. Mater.* **2012**, *22*, 1333.

[29] A. Kanitz, M. R. Kalus, E. L. Gurevich, A. Ostendorf, S. Barcikowski, D. Amans, *Plasma Sources Sci. Technol* **2019**, *28*, 103001.

[30] M. D. Shirk, P. A. Molian, *J. Laser Appl.* **1998**, *10*, 18.

[31] W. An, J. Fu, S. Mei, L. Xia, X. Li, H. Gu, X. Zhang, B. Gao, P. K. Chu, K. Huo, *J. Mater. Chem. A* **2017**, *5*, 14422.

[32] H. Luo, C. Gu, W. Zheng, F. Dai, X. Wang, Z. Zheng, *RSC Adv.* **2015**, *5*, 13470.

[33] X. Yang, J. Ma, H. Wang, Y. Chai, R. Yuan, *Mater. Chem. Phys.* **2018**, *213*, 208.

[34] K.-S. Hong, D.-H. Nam, S.-J. Lim, D. Sohn, T.-H. Kim, H. Kwon, *ACS Appl. Mater. Interfaces* **2015**, *7*, 17264.
[35] M. Deng, S. Li, W. Hong, Y. Jiang, W. Xu, H. Shuai, G. Zou, Y. Hu, H. Hou, W. Wang, X. Ji, *Mater. Chem. Phys.* **2019**, *223*, 46.
[36] J. Gong, G. Zhao, J. Feng, Y. An, T. Li, L. Zhang, B. Li, Z. Qian, *ACS Nano* **2020**, *14*, 14057.
[37] M. J. Matthews, M. A. Pimenta, G. Dresselhaus, M. S. Dresselhaus, M. Endo, *Phys. Rev. B* **1999**, *59*, R6585.
[38] A. Jorio, A. G. Souza Filho, G. Dresselhaus, M. S. Dresselhaus, A. K. Swan, M. S. Ünlü, B. B. Goldberg, M. A. Pimenta, J. H. Hafner, C. M. Lieber, R. Saito, *Phys. Rev. B* **2002**, *65*, 155412.
[39] X. Lin, J. Huang, B. Zhang, *Carbon* **2019**, *143*, 138.
[40] B. Zhang, C. M. Ghimbeu, C. Laberty, C. Vix-Guterl, J.-M. Tarascon, *Adv. Energy Mater.* **2016**, *6*, 1501588.
[41] B. Zhang, Y. Yu, Z.-L. Xu, S. Abouali, M. Akbari, Y.-B. He, F. Kang, J.-K. Kim, *Adv. Energy Mater.* **2014**, *4*, 1301448.
[42] W. Ma, J. Wang, H. Gao, J. Niu, F. Luo, Z. Peng, Z. Zhang, *Energy Stor. Mater.* **2018**, *13*, 247.
[43] H. Bryngelsson, J. Eskhult, L. Nyholm, M. Herranen, O. Alm, K. Edström, *Chem. Mater.* **2007**, *19*, 1170.
[44] H. Yang, R. Xu, Y. Yao, S. Ye, X. Zhou, Y. Yu, *Adv. Funct. Mater.* **2019**, *29*, 1809195.
[45] Z. Zhu, S. Wang, J. Du, Q. Jin, T. Zhang, F. Cheng, J. Chen, *Nano Lett.* **2014**, *14*, 153.
[46] S. M. Beladi-Mousavi, S. Sadaf, L. Walder, M. Gallei, C. Rüttiger, S. Eigler, C. E. Halbig, *Adv. Energy Mater.* **2016**, *6*, 1600108.
[47] E. Dickinson, *J. Chem. Technol. Biotechnol.* **1989**, *45*, 328.
[48] Y.-Y. Lin, Y.-M. Chen, S.-S. Hou, J.-S. Jan, Y.-L. Lee, H. Teng, *J. Mater. Chem. A* **2017**, *5*, 17476.
[49] A. Jain, S. P. Ong, G. Hautier, W. Chen, W. D. Richards, S. Dacek, S. Cholia, D. Gunter, D. Skinner, G. Ceder, K. A. Persson, *APL Mater.* **2013**, *1*, 011002.
[50] J. Zheng, Y. Wu, Y. Sun, J. Rong, H. Li, L. Niu, *Nano-Micro Lett.* **2020**, *13*, 12.
[51] J. H. Ku, J. H. Ryu, S. H. Kim, O. H. Han, S. M. Oh, *Adv. Funct. Mater.* **2012**, *22*, 3658.
[52] Y.-R. Zhu, Y. Xie, R.-S. Zhu, J. Shu, L.-J. Jiang, H.-B. Qiao, T.-F. Yi, *Ionics* **2011**, *17*, 437.
[53] D. Qu, G. Wang, J. Kafle, J. Harris, L. Crain, Z. Jin, D. Zheng, *Small Methods* **2018**, *2*, 1700342.
[54] Y. Zhu, C. Wang, *J. Phys. Chem. C* **2010**, *114*, 2830.
[55] Z. Shen, L. Cao, C. D. Rahn, C.-Y. Wang, *J. Electrochem. Soc.* **2013**, *160*, A1842.
[56] J. Song, P. Yan, L. Luo, X. Qi, X. Rong, J. Zheng, B. Xiao, S. Feng, C. Wang, Y.-S. Hu, Y. Lin, V. L. Sprenkle, X. Li, *Nano Energy* **2017**, *40*, 504.
[57] M. Hu, Y. Jiang, W. Sun, H. Wang, C. Jin, M. Yan, *ACS Appl. Mater. Interfaces* **2014**, *6*, 19449.
[58] J. Li, N. Zhuang, J. Xie, X. Li, W. Zhuo, H. Wang, J. B. Na, X. Li, Y. Yamauchi, W. Mai, *Adv. Energy Mater.* **2020**, *10*, 1903455.
[59] H. Zhang, X. Huang, O. Noonan, L. Zhou, C. Yu, *Adv. Funct. Mater.* **2017**, *27*, 1606023.
[60] H. Tan, D. Chen, X. Rui, Y. Yu, *Adv. Funct. Mater.* **2019**, *29*, 1808745.
[61] Q. Cai, X. Li, E. Hu, Z. Wang, P. Lv, J. Zheng, K. Yu, W. Wei, K. Ostrikov, *Small* **2022**, *18*, 2200694.
[62] Q. Zhang, Y. Zeng, C. Ling, L. Wang, Z. Wang, T.-E. Fan, H. Wang, J. Xiao, X. Li, B. Qu, *Small* **2022**, *18*, 2107514.
[63] R. Zhao, H. Di, C. Wang, X. Hui, D. Zhao, R. Wang, L. Zhang, L. Yin, *ACS Nano* **2020**,

14, 13938.
[64] B. Chen, L. Yang, X. Bai, Q. Wu, M. Liang, Y. Wang, N. Zhao, C. Shi, B. Zhou, C. He, *Small* **2021**, *17*, 2006824.
[65] E. Uchaker, Y. Z. Zheng, S. Li, S. L. Candelaria, S. Hu, G. Z. Cao, *J. Mater. Chem. A* **2014**, *2*, 18208.
[66] Z. Wei, D. Wang, X. Yang, C. Wang, G. Chen, F. Du, *Adv. Mater. Interfaces* **2018**, *5*, 1800639.
[67] A. Darwiche, L. Bodenes, L. Madec, L. Monconduit, H. Martinez, *Electrochim. Acta* **2016**, *207*, 284.
[68] Y. Liu, N. Zhang, C. Yu, L. Jiao, J. Chen, *Nano Lett.* **2016**, *16*, 3321.
[69] Y. Zhang, H. Tao, S. Du, X. Yang, *ACS Appl. Mater. Interfaces* **2019**, *11*, 11327.

Figures

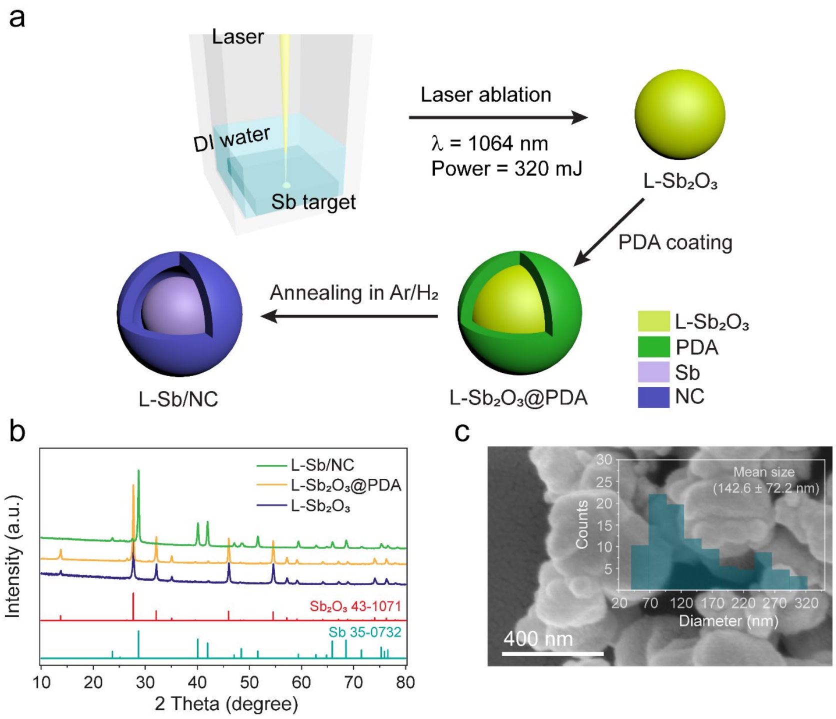

Figure 1. (a) Schematic illustration showing the fabrication process of L-Sb/NC. (b) XRD patterns of L-Sb_2O_3, L-Sb_2O_3@PDA, and L-Sb/NC. (c) SEM image of L-Sb/NC. Inset in (c) shows the size distribution of as-fabricated L-Sb/NC.

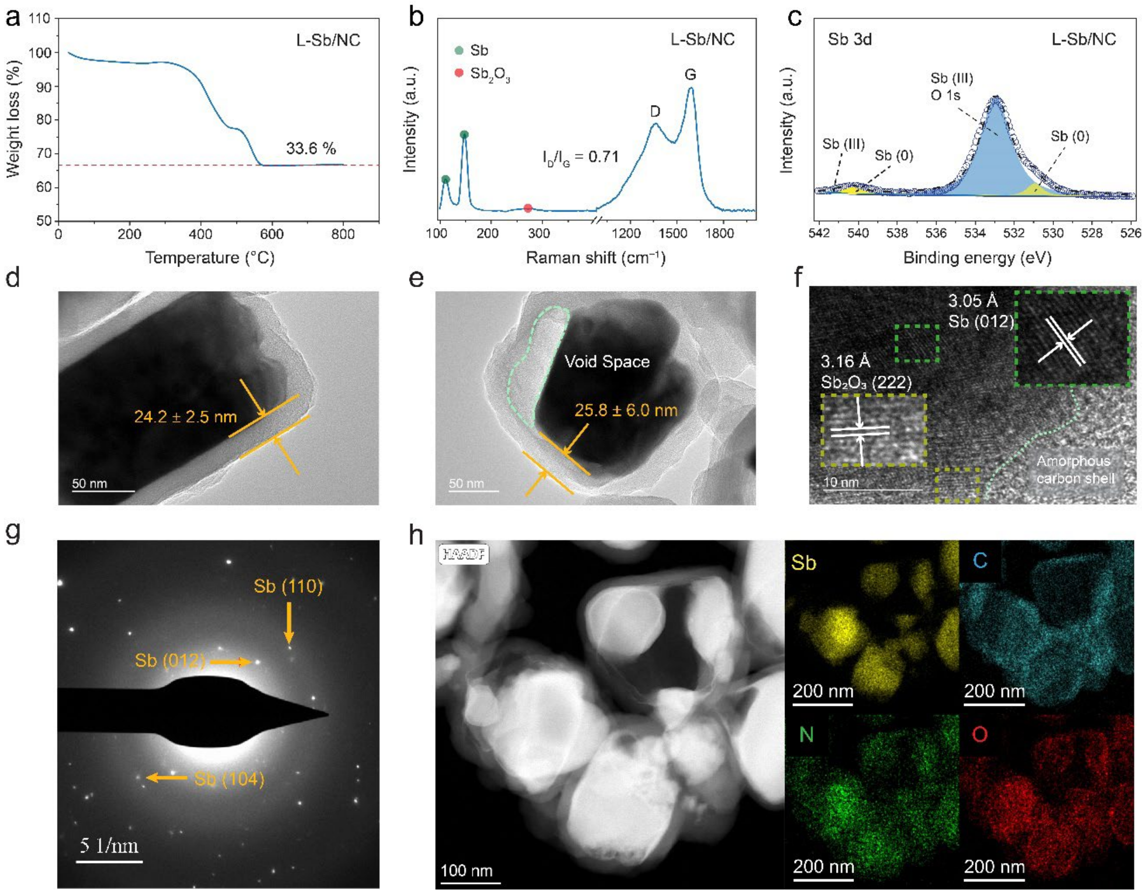

Figure 2. (a) Thermogravimetric analysis, (b) Raman spectrum, and (c) Sb 3*d* XPS spectrum of L-Sb/NC. TEM images of (d) L-Sb_2O_3@PDA and (e) L-Sb/NC. (f) HRTEM image, (g) SAED pattern, and (h) STEM image of L-Sb/NC with the corresponding elemental distributions.

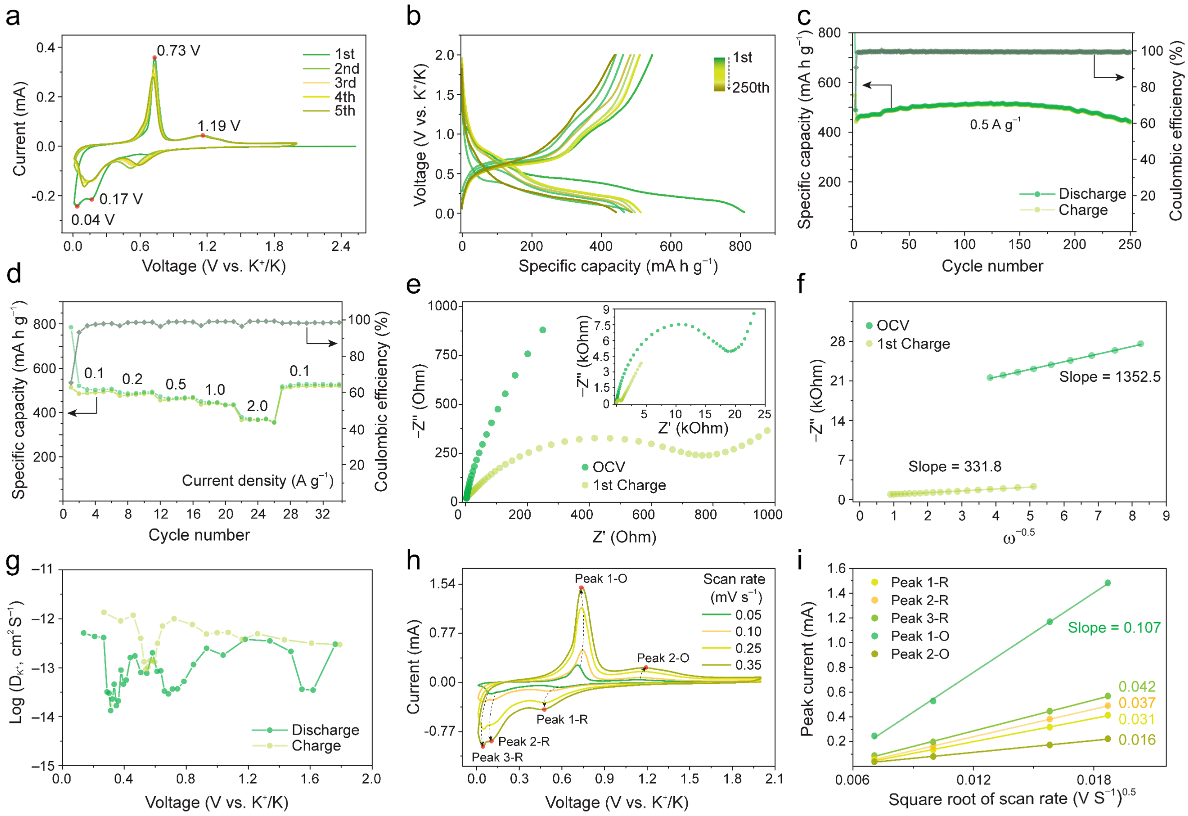

Figure 3. Electrochemical properties of L-Sb/NC for PIB. (a) CVs at a scan rate of 0.05 mV s^{-1}. (b) Discharge/charge curves in various cycles at 0.5 A g^{-1} within 0.01 − 2.0 V (*vs.* K^+/K). (c) Cycle performance at 0.5 A g^{-1} and (d) rate capability at various current densities. Comparison of pristine and first-cycled cells: (e) Nyquist plots and (f) relationship of Z' and $\omega^{-1/2}$ in the low-frequency range. (g) Diffusion coefficients for K^+ ions as a function of voltage calculated from the GITT profiles (**Figure S12**) during the 1st discharge and charge process. (h) CVs of L-Sb/NC electrode at scan rates of 0.05, 0.10, 0.25, and 0.35 mV s^{-1} within 0.01 − 2.0 V (*vs.* K^+/K). (i) Linear relationship of peak current and the square root of scan rate.

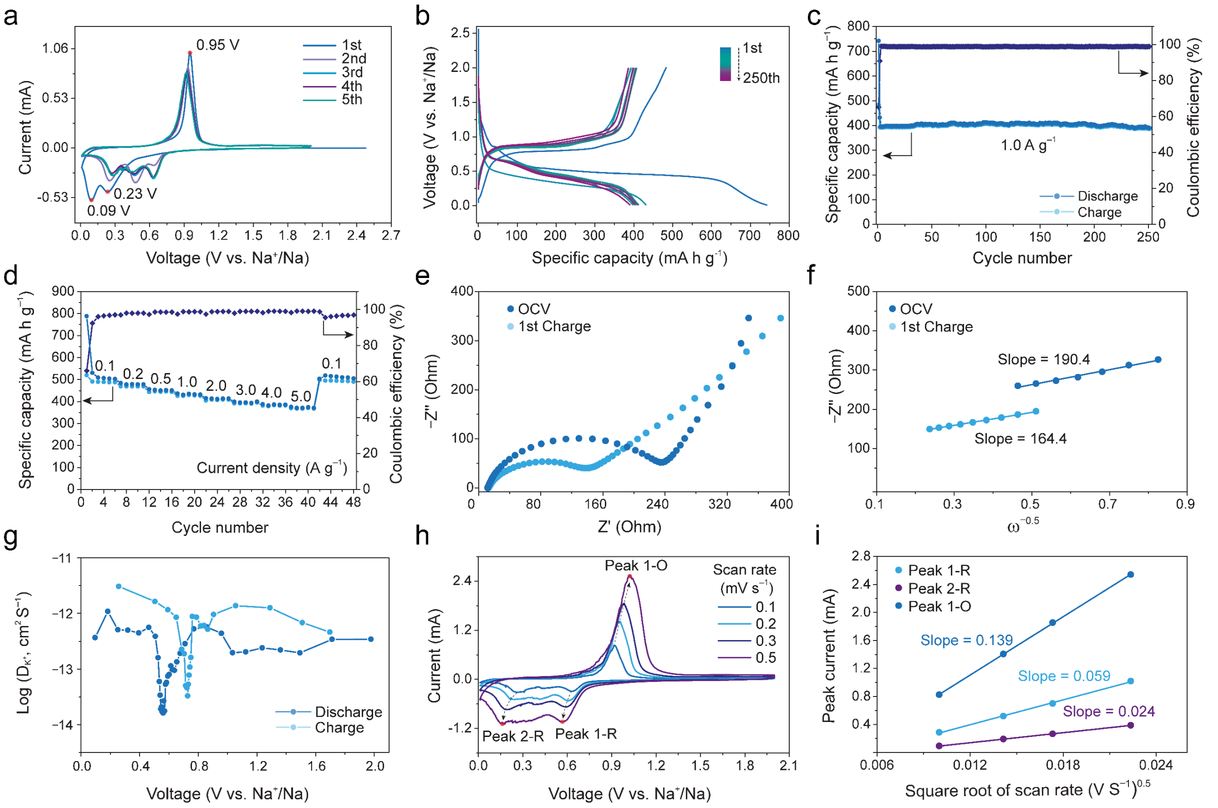

Figure 4. Electrochemical properties of L-Sb/NC for SIB. (a) CVs at a scan rate of 0.1 mV s^{-1}. (b) Discharge/charge curves in various cycles at 1.0 A g^{-1} within 0.01 − 2.0 V (*vs.* Na^+/Na). (c) Cycle performance at 1.0 A g^{-1} and (d) rate capability at various current densities. Comparison of pristine and first-cycled cells: (e) Nyquist plots and (f) relationship of Z' and $\omega^{-1/2}$ in the low-frequency range. (g) Diffusion coefficients for Na^+ ions as a function of voltage calculated from the GITT profiles (**Figure S15**) during the 1st discharge and charge process. (h) CVs of L-Sb/NC electrode at scan rates of 0.1, 0.2, 0.3, and 0.5 mV s^{-1} within 0.01 − 2.0 V (*vs.* Na^+/Na). (i) Linear relationship of peak current and the square root of scan rate.

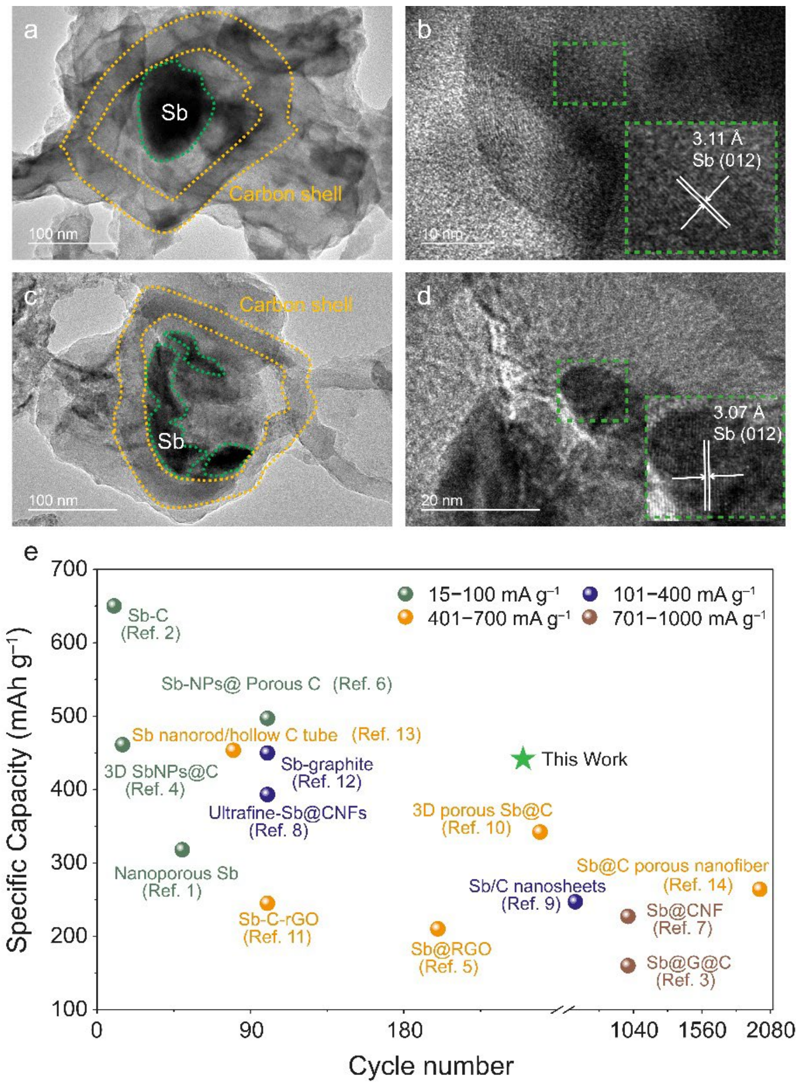

Figure 5. TEM images of L-Sb/NC electrode after 100 cycles in (a,b) PIB and (c,d) SIB. (e) Cycle performances of L-Sb/NC PIB in comparison with recently reported Sb-based PIBs. Data are summarized in **Table S5**.

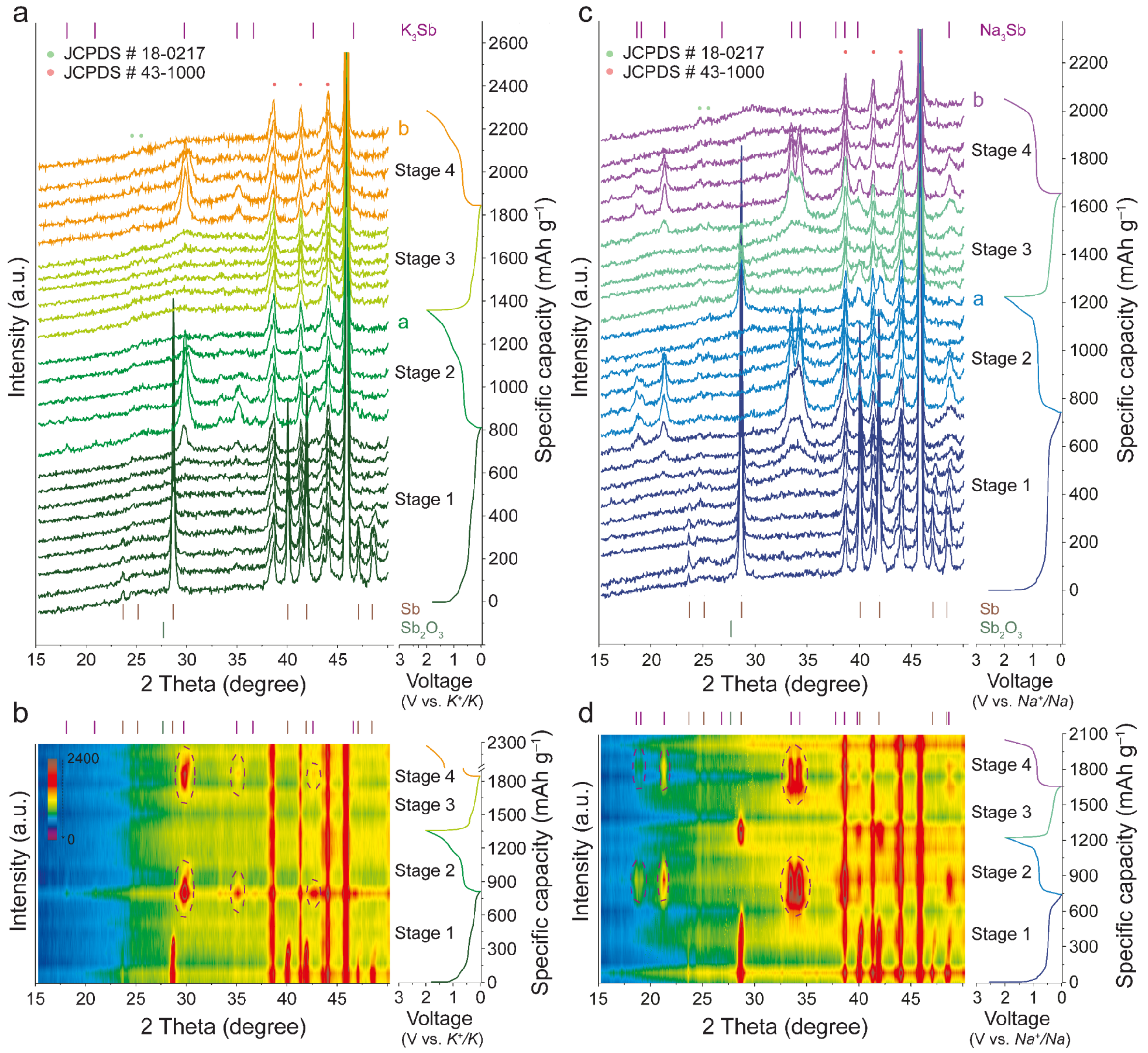

Figure 6. (a,c) Line plot and (b,d) contour plot of *operando* XRD of L-Sb/NC electrode during the initial two cycles in (a,b) PIB and (c,d) SIB. Discharge–charge profiles at 0.05 A g^{-1} are tested, and BeO (JCPDS # 43-1000) and Be$_{11}$Fe (JCPDS # 18-0217) peaks are labelled with green and orange dots in line plots.

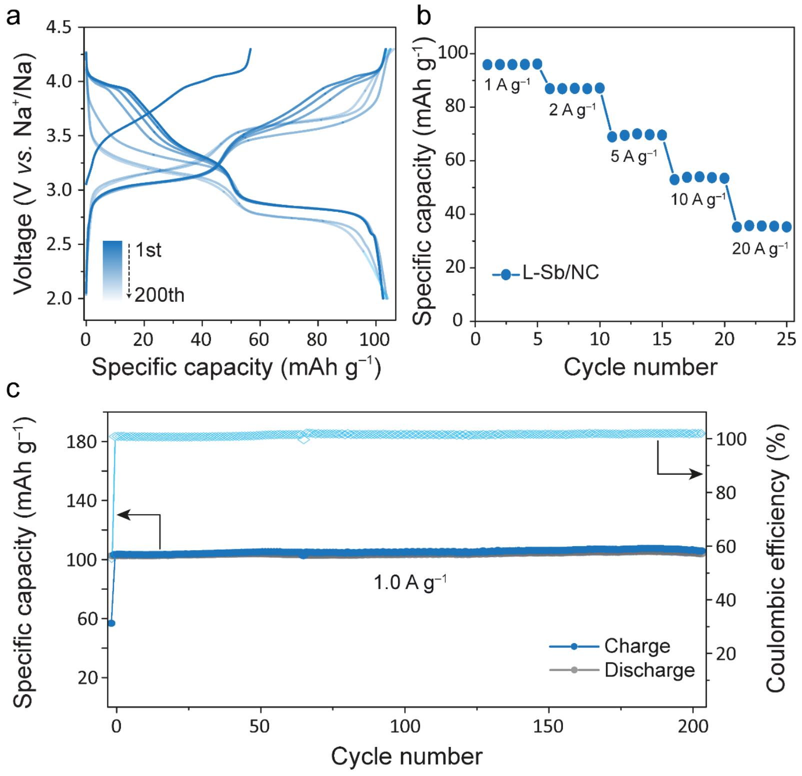

Figure 7. Electrochemical performances of full battery constructed with L-Sb/NC anode and $Na_3V_2(PO_4)_2F_3$ cathode. (a) Charge–discharge curves, (b) rate capability at various current densities, and (c) cycle performance in the potential range of 2.0 − 4.3 V (*vs.* Na^+/Na) at a current density of 1.0 A g^{-1}.